SCIENTIFIC REPORTS

OPEN

SUBJECT AREAS:
NANOPHOTONICS AND PLASMONICS
OPTICAL PROPERTIES AND DEVICES

Received
30 May 2014

Accepted
12 September 2014

Published
9 October 2014

Correspondence and requests for materials should be addressed to M.G. (mgu@swin.edu.au)

* These authors contributed equally to this work.

Graphene surface plasmons at the near-infrared optical regime

Qiming Zhang[1,2]*, Xiangping Li[1]*, Md Muntasir Hossain[2], Yunzhou Xue[3], Jie Zhang[3], Jingchao Song[4], Jingying Liu[4], Mark D. Turner[1], Shanhui Fan[5], Qiaoliang Bao[3,4] & Min Gu[1,2]

[1]Centre for Micro-Photonics, Faculty of Science, Engineering and Technology, Swinburne University of Technology, Hawthorn, Victoria 3122, Australia, [2]Centre for Micro-Photonics and CUDOS, Faculty of Science, Engineering and Technology, Swinburne University of Technology, Hawthorn, Victoria 3122, Australia, [3]Institute of Functional Nano and Soft Materials (FUNSOM), and Collaborative Innovation Center of Suzhou Nano Science and Technology, Soochow University, Suzhou 215123, China, [4]Department of Materials Engineering, Faculty of Engineering, Monash University, Clayton, Victoria 3800, Australia, [5]Department of Electrical Engineering, Stanford University, Stanford, California 94305, USA.

Graphene has been identified as an emerging horizon for a nanoscale photonic platform because the Fermi level of intrinsic graphene can be engineered to support surface plasmons (SPs). The current solid back electrical gating and chemical doping methods cannot facilitate the demonstration of graphene SPs at the near-infrared (NIR) window because of the limited shift of the Fermi level. Here, we present the evidence for the existence of graphene SPs on a tapered graphene-silicon waveguide tip at a NIR wavelength, employing a surface carrier transfer method with molybdenum trioxides. The coupling between the graphene surface plasmons and the guiding mode in silicon waveguides allows for the observation of the concentrated field of the SPs in the tip by near-field scanning optical microscopy. Thus the hot spot from the concentrated SPs in the graphene layer can be used as a key experimental signature of graphene SPs. The NIR graphene SPs opens a new perspective for optical communications, optical sensing and imaging, and optical data storage with extreme spatial confinement, broad bandwidth and high tunability.

The high carrier mobility, which originates from the fact that free carriers in graphene behave as massless Dirac Fermions[1], makes graphene a good candidate for SPs at broad bands[2–8]. Intrinsic graphene cannot support SPs due to its low carrier density. However, the atomically thin nature of graphene provides the exciting opportunity of increasing the free carrier density by tuning its Fermi level through either an electric gating or chemical doping[9–17]. The conventional solid back electric gating method can lift or lower the Fermi level of intrinsic graphene through the electron injection (n-type doping) or hole injection (p-type doping)[18]. However, the achieved doping level is low as limited by the breakdown of the dielectric material of the gating, which restricts the operating wavelengths of SPs to the range from terahertz to mid-infrared[11–13]. A larger Fermi level shift is possible with an ion gel layer[19]; however, the replacement of air with the thick ion gel layer on top of graphene limits the application of the devices. Alternatively, a high doping level can be achieved through chemical doping by the surface treatment induced defects without a thick cladding layer[14,20,21]. A shift of 1 eV of Fermi level is even possible by chemical doping with intercalating few-layer graphene with ferric chloride[22]. However, the interaction between the layers changes the electronic properties of single layer graphene, and tampers the condition for supporting SPs.

Here, we present the first observation of graphene SPs on a tapered graphene-silicon waveguide tip at a NIR wavelength, through lifting its Fermi level using a surface carrier transfer method with molybdenum trioxides (MoO_3). A thin layer of molybdenum trioxides was deposited on top of the graphene layer (Fig. 1a). The electron affinity arising from the difference in work functions drives the surface electron injection from the graphene layer to the MoO_3 layer, when these materials are located in a close proximity[23,24]. Thus, the graphene layer becomes p-doped with free holes. The shift of the Fermi level induced by surface carrier transfer can change the equilibrium lattice parameter and the phonon dispersion in graphene[25,26]. Specifically, the lattice of graphene contracts as the free hole density increases. Thus, the strong phonon-hole coupling in graphene results in a corroborative connection between the Raman spectra and the electronic structure[27], which allows one to directly determine the Fermi level by Raman spectroscopy.

Even though the carrier density in graphene can be increased to support graphene SPs at the NIR regime, the observation of NIR SPs remains a major challenge due to the low coupling efficiency associated with the small mode area of graphene SPs. In addition, the effective wavelength of graphene SPs excited at a NIR wavelength is at

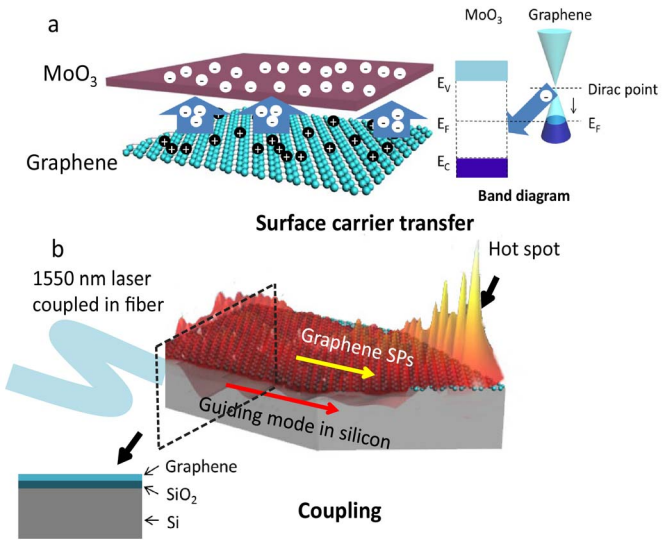

Figure 1 | Schematic of the demonstration of graphene SPs at a NIR wavelength. (a). Schematic of the surface carrier transfer of graphene with MoO_3. The inset on the right shows the energy-band diagram of graphene and MoO_3. (b). Schematic illustration of the coupling of graphene SPs and the guiding mode in silicon waveguides in a tapered geometry.

a scale of ~10 nm^2, which is beyond the resolution capability of current optical characterization systems. The desirable strong confinement of SPs is associated with an extremely large wave vector, which makes the efficient coupling of graphene SPs difficult, and thus presents an obstacle for the observation. To overcome these problems, we couple the graphene SPs with the guiding mode in silicon waveguides, as achieved by placing a mono-layer of graphene on top of a silicon waveguide (Fig. 1b). This is similar to plasmonic nanostructures integrated with dielectric structures to achieve coupling between the plasmonic and dielectric guiding modes[28–30]. Consequently, the coupling of graphene SPs and the guiding mode in silicon waveguides allows for the efficient excitation of graphene SPs by a fiber coupling method. The tapered geometry at the end of the waveguide results in the strong plasmonic field confinement at the apex of the tip end. Thus the emergence of such a hot spot from the concentrated SPs in the graphene layer can be used as a key experimental signature of graphene SPs.

The graphene-silicon waveguide was fabricated by nanofabrication on a silicon-on-insulator (SOI) wafer (see Methods and Supplementary Section S1). The thickness of the silicon layer was 260 nm. A thin layer of SiO_2 of 3 nm was grown on top of the silicon layer to separate the graphene layer from the silicon layer. A mono-layer graphene grown by the chemical vapour deposition (CVD) method was then wet-transferred onto the top of the silicon waveguide. A 6 nm thick layer of MoO_3 was deposited on the top of the graphene layer for the surface carrier transfer process, which was measured by the quartz crystal microbalance sensor during the deposition process. The surface roughness (Ra = 0.52 nm) after the deposition was confirmed to be negligibly small by an atomic force microscope (AFM) (inset of Fig. 2a). The propagation length of the mode at a free-space wavelength of 1550 nm in the straight silicon-graphene waveguide is strongly enhanced after the surface carrier transfer to shift the Fermi level of the graphene layer (see Supplementary Section S2). The enhanced propagation length allows us to design the tapered waveguide structure for concentrating SPs at the tip end. The scanning electron microscope (SEM) images of the resulting structure are shown in Fig. 2a. The tapered graphene-silicon waveguide tip has a width of 2 μm in the uniform region and a length of 8 μm. The apex diameter of the tapered tip was 36 ± 2 nm. It should be noted that the orientation and quality of the edges of graphene start to influence the surface plasmons once the size of the

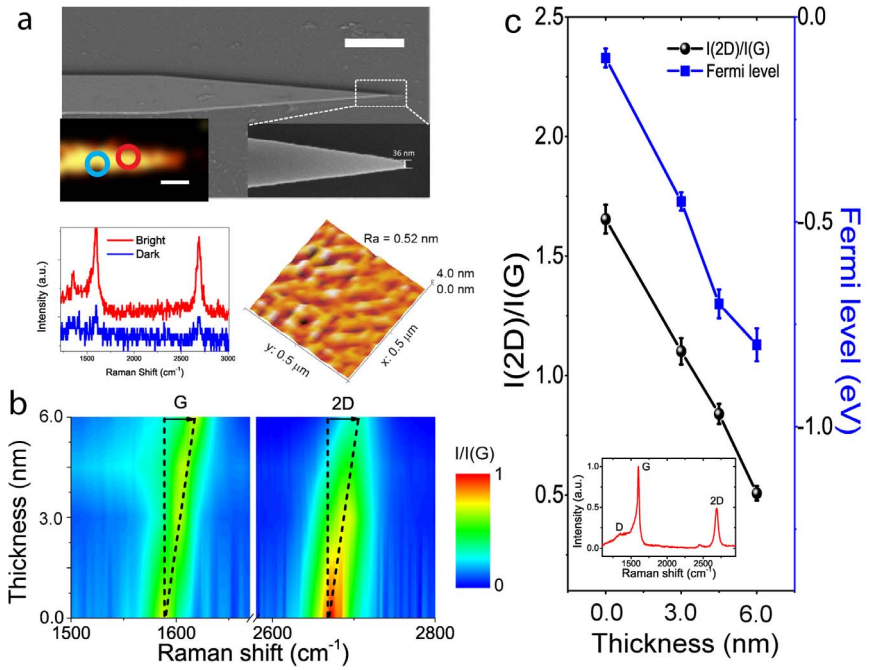

Figure 2 | Determination of the Fermi level of the graphene layer. (a). SEM images of a tapered graphene-silicon waveguide tip. Scale bar: 4 μm. Inset: Middle left: Raman G peak image of tapered graphene-silicon waveguide tips. Scale bar: 2 μm. Middle right: SEM images of the zoom-in view of the tapered graphene-silicon waveguide tip. Bottom left: Raman signal of the dark and bright region in the Raman mapping. Bottom right: AFM images of the surface of the MoO_3 with a thickness of 6 nm. (b). Raman spectra of the graphene layer normalized to I(G) before and after the surface carrier transfer with MoO_3. (c). Fermi level and I(2D)/I(G) of graphene for different MoO_3 deposition times. Inset: Raman spectra of the graphene layer after surface carrier transfer with MoO_3 showing a Fermi level shift of −0.8 eV.

graphene coated silicon tip is further decreased to a few nanometers[31].

To confirm the changes of the Fermi level after the surface carrier transfer, we measured the Raman spectra of the graphene layer (see Methods). Both the SEM images and the Raman G peak image (inset of Fig. 2a) clearly indicate that the graphene layer has been covered on top of the tapered silicon waveguide tip. The slight inhomogeneity in the Raman mapping is likely due to residue PMMA composites that change the strength of the Raman signals. The Raman spectra for both the dark and bright parts in the Raman mapping exhibit the characteristics of graphene as shown in the inset of the Fig. 2a, which confirms the continuity of the graphene layer. Fig. 2b reveals the shifts of the Raman spectra after the deposition of the MoO_3 layer. The 2D peak at $\sim$2670 cm^{-1} involving phonons near the K point in the first brillouin zone of graphene is sensitive to the lattice constant of graphene and thus allows the use of the 2D peak shift to distinguish between electron and hole doping[32]. The observation of the upshift of the 2D peak from 2670 cm^{-1} to 2690 cm^{-1} in our experiment indicates a p-type doping with an increased free hole density[32].

The G peak at $\sim$1587 cm^{-1} involving phonons near the Γ point in the first brillouin zone is sensitive to the absolute value of the Fermi level due to the modification of the phonon dispersion close to Kohn anomalies[33]. The dependence of the Fermi level of the 2D mode is much stronger than that of the G mode. The ratio of the intensity of the 2D peak (I(2D)) to the intensity of the G peak (I(G)) exhibits a clear dependence on the Fermi level, and can be used to determine the level of doping in graphene[32]. Based on the dependence of the I(2D)/I(G) on the Fermi level in an electric gating experiment of a graphene transistor[25,32], the shifts of the Fermi level can be projected from I(2D)/I(G) as shown in Fig. 2c. The I(2D)/I(G) changes to 0.5 after the surface carrier transfer, corresponding to a down-shift of 0.8 eV in the Fermi level (E_F) when the thickness of the MoO_3 layer is 6 nm (Fig. 2c). The changes of the Fermi level can also be determined from the upshift of the G peak and the changes in the ultraviolet photoelectron spectroscopy, which is consistent with the result determined from the I(2D)/I(G) (see Supplementary Section S2). As a consequence, the Fermi level changed greater than 0.6 eV after the surface carrier transfer with MoO_3 can allow graphene SPs at the NIR wavelength of 1550 nm at the experimental condition (Supplementary Section S4). The slight asymmetry of the G peak after doping might be attributed to the local inhomogeneity of doping[34].

Based on the Fermi level determined in the experiment, the effective mode index of the TM polarized graphene SPs in different Fermi levels as a function of the waveguide width can be calculated by the eigen-mode solver with the finite element method on the 2D cross-sectional geometry. The complex permittivity of graphene is calculated with Kubo formula and the graphene layer is considered as a thin film with a thickness of 0.5 nm (see Methods). Fig. 3a shows the simulated effective mode index (n_{eff}) of the graphene SP mode in different Fermi levels. The effective mode index of the graphene SPs decreases as the absolute value of Fermi level increases. The effective mode index of the TM polarized guiding mode in silicon waveguides is also presented in Fig. 3a for comparison. Due to the strong confinement of graphene SPs, the graphene layers can support modes at a width much smaller than the cutoff width of the guiding mode in silicon waveguides. Consequently, a hot spot at the end of the tapered graphene-silicon waveguide tip can be observed only if the graphene SPs can be excited efficiently.

The excitation efficiency of graphene SPs can be enhanced by the coupling between the graphene SPs and the guiding mode in silicon waveguides. The graphene SPs and the guiding mode in silicon waveguides couples when the graphene layer and the silicon layer are in the close proximity (see Supplementary Section S4). The fraction of power coupled into graphene SP mode gradually increases as the absolute value of the Fermi level increases. This is due to a smaller effective mode index mismatch between the silicon waveguide mode and the graphene SPs with a higher doping level. Thus, the graphene SPs can be excited by using conventional coupling methods such as fiber coupling. In order to demonstrate this, a three-dimensional simulation of light propagation through the tapered graphene-silicon waveguide tip with different Fermi levels is carried out by the finite element method (See Methods). A plane wave polarized perpendicular to the plane of the graphene surface is excited at the end facet at a free space wavelength of 1550 nm for the excitation of TM mode. The intensity distributions in the cross section in the YZ plane in the center of the tapered graphene-silicon waveguide tip are shown in Fig. 3b. As the absolute value of Fermi level increases, the intensity near the graphene layer at the end of the tip increases. This is also evident in cross section XY plane as graphene SPs are concentrated at the end of the tip (Fig. 3c). Consequently, a highly enhanced field at the sharp tip of the tapering end arising from the concentrated graphene SPs can be observed, which cannot be achieved in dielectric tapered structures due to the cutoff.

The simulation result of the intensity distribution on top of the graphene layer is shown in Fig. 4a. The result is convoluted with the point-spread function of the near-field scanning optical microscopy (NSOM) probe by considering the resolution of the optical system. As light propagates along the z axis, the intensity begins to drop at the position of $\sim$700 nm with respect to the apex of the tip, where the width of the tip is around 200 nm. The decay of intensity along the tapered tips can be attributed to the cutoff of the guiding mode in silicon waveguides at this critical width. Similarly, the intensity starts to decay at the same tip width in the simulation of the tapered tip without graphene, as shown in Fig. 4b. The simulation shows that the hot spot related to the changes of Fermi level of the graphene layer appears at a position $\sim$100 nm away from the end of the tip due to the strong spatial confinement of graphene SPs. The intensity of the cross section along the x and z directions reveals an enhancement of the intensity owing to the concentrated graphene SPs compared with the waveguide without the graphene layer (Figs. 4e and 4f). In addition, the intensity of the hotspot increases as the absolute value of the Fermi level increases owing to a higher coupling efficiency (Fig. 4g).

In order to confirm the simulation result, we carried on the near-field characterization of the tapered graphene-silicon waveguide tip using a NSOM (see Supplementary Section S2). Indeed, a hot spot appear in the graphene-silicon waveguide tip after the surface carrier transfer with MoO_3 to shift the Fermi level by -0.8 eV (Fig. 4c). The consistency of the intensity profile and the intensity ratio compared with the sample without graphene (I(with Gr)/I(w/o Gr)) between the simulation and the experimental results confirms that the hot spot originates from the confinement of graphene SPs (Figs. 4e–g). In contrast, no hot spot is observed at the end of the tapered silicon waveguide tip without graphene (Fig. 4d and 4f). The full width at half maximum (FWHM) of hot spot is measured $\sim$180 nm limited by the spatial resolution of the NSOM probe.

To verify the polarization property of the surface plasmons in graphene, we carried out more control experiments by coupling light at different polarization states. Under illumination where the electric field is along the plane of the graphene surface to excite the transverse electric (TE) mode, it can be seen that the near-field distribution of the tapered graphene-silicon waveguide tip is almost identical to that without the graphene layer due to the lack of supporting graphene SPs at this polarization state.

The influence of the thin layer deposition of MoO_3 on the cutoff of the tapered silicon waveguide can be excluded since no hot spot at the end of the tip can be observed in the MoO_3 coated silicon tip without graphene under TM polarization (see Supplementary Section S6). Meanwhile, the numerical simulation reveals that the surface roughness of the silicon layer and the MoO_3 layer has a negligible effect on the concentrated hot spot at the end of the tapered tip. (see Supplementary Sections S7). Thus, these results led to the solid con-

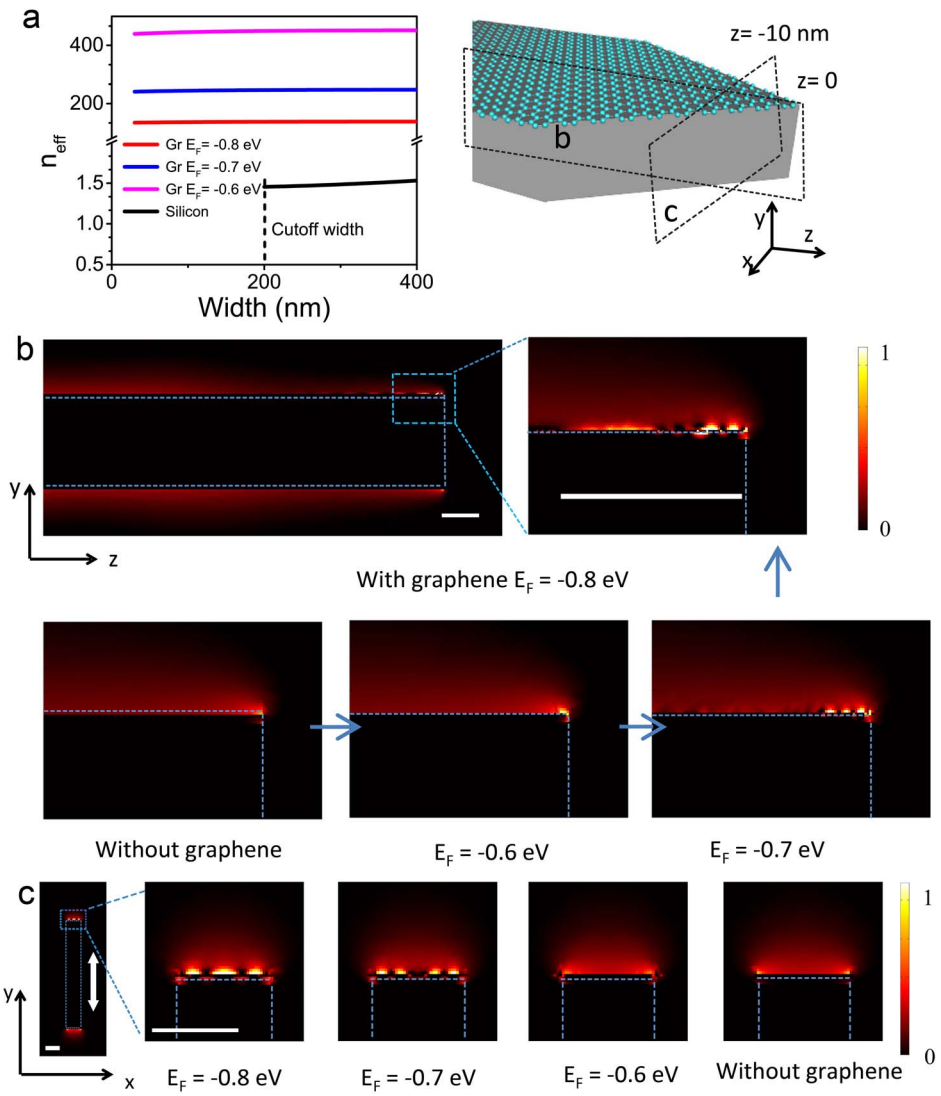

Figure 3 | Simulation result of the light propagation in the tapered graphene-silicon waveguide tip. (a). Effective mode index (n_{eff}) of the graphene SP modes, and the guiding mode in silicon waveguides. Gr denotes graphene. (b). Simulation results of intensity distributions at YZ cross section of the tapered graphene-silicon waveguide tips and tapered silicon waveguide tips under TM polarization illumination. Scale bar: 100 nm. (c). Simulation results of intensity distributions at XY cross section of the tapered graphene-silicon waveguide tips and tapered silicon waveguide tips under TM polarization illumination. Scale bar: 35 nm. The input polarization direction is indicated on the bottom right corner.

clusion that the appearance of the hot spot at the end of the tapered tip can be attributed to the presence of graphene SPs at the NIR regime. In the future, a high resolution NSOM beyond 10 nm may provide a direct evidence to the graphene SPs through directly mapping the wavelength and the lifetime of SPs. The proposed surface carrier transfer method opens new perspective for extending graphene SPs to NIR regimes, even possible to visible windows. The demonstrated approach combining its unique properties of broad bands and tunability may further spur the development of graphene-based plasmonic devices with a deep sub-wavelength confinement for a wide range of optical applications[3,35–42].

Methods

The silicon waveguide was fabricated with a silicon-on-insulator (SOI) wafer (Soitec). A pattern was formed on a resist layer coated on top of the wafer by Ebeam lithography (EBPG 5000, Vistec). Then the pattern was transferred to the chromium layer by the lift-off process. The chromium layer served as a hard mask for the reactive ion etching of the silicon layer with a mixed gas process (C_4F_8 and SF_6). Then the chromium layer was removed by a chromium etchant (Transene). A SiO_2 layer of 3 nm was grown on top of the silicon layer by the atomic layer deposition. The single layer graphene grown on copper by the CVD method was then wet-transferred onto top of the silicon waveguide (see Supplementary Section S1).

The Raman spectra and images were measured on WITEC Alpha 300 confocal micro-Raman system equipped with a 532 nm laser source and 100× objective lens. The surface morphology of MoO_3-coated graphene films was characterized with AFM (Veeco Multimode V) in the tapping mode. The SEM image was captured on FEI NovaNanoSEM 430 scanning electron microscopy.

The simulation results of the effective mode index and the field distribution in Fig. 3a, Fig. S4, Fig. S6, Fig. S7 and Fig. S10 are calculated by the eigen-mode solver of finite element method (Comsol) on the 2D cross-sectional geometry. The simulation results of the mode distribution in Figs. 3b–c, Figs. 4a–b, Figs. 4e–g, Fig. S9b and Fig. S12 are calculated by the finite element method (CST) on the 3D tapered structure geometry. The complex permittivity of graphene is calculated using the Kubo formula[43,44] and the graphene layer is considered as a thin film with a thickness of 0.5 nm[9] (see Supplementary Section S4). The frequency dependent optical conductivity (σ) of graphene considering both the interband and intraband optical transitions is calculated by

$$\sigma = \frac{je^2|E_F|}{\pi\hbar^2(\omega + j\tau^{-1})} + \frac{je^2}{4\pi\hbar}\ln\left(\frac{2|E_F| - (\omega + j\tau^{-1})\hbar}{2|E_F| + (\omega + j\tau^{-1})\hbar}\right) \quad (1)$$

where e is the electron charge, $\hbar$ is the reduced Planck's constant, ω is the angular frequency, E_F is the Fermi level and τ is the relaxation time. By considering the carrier-phonon scattering[1], a relaxation time of 0.03 ps consistent with the literature is used in the simulation.

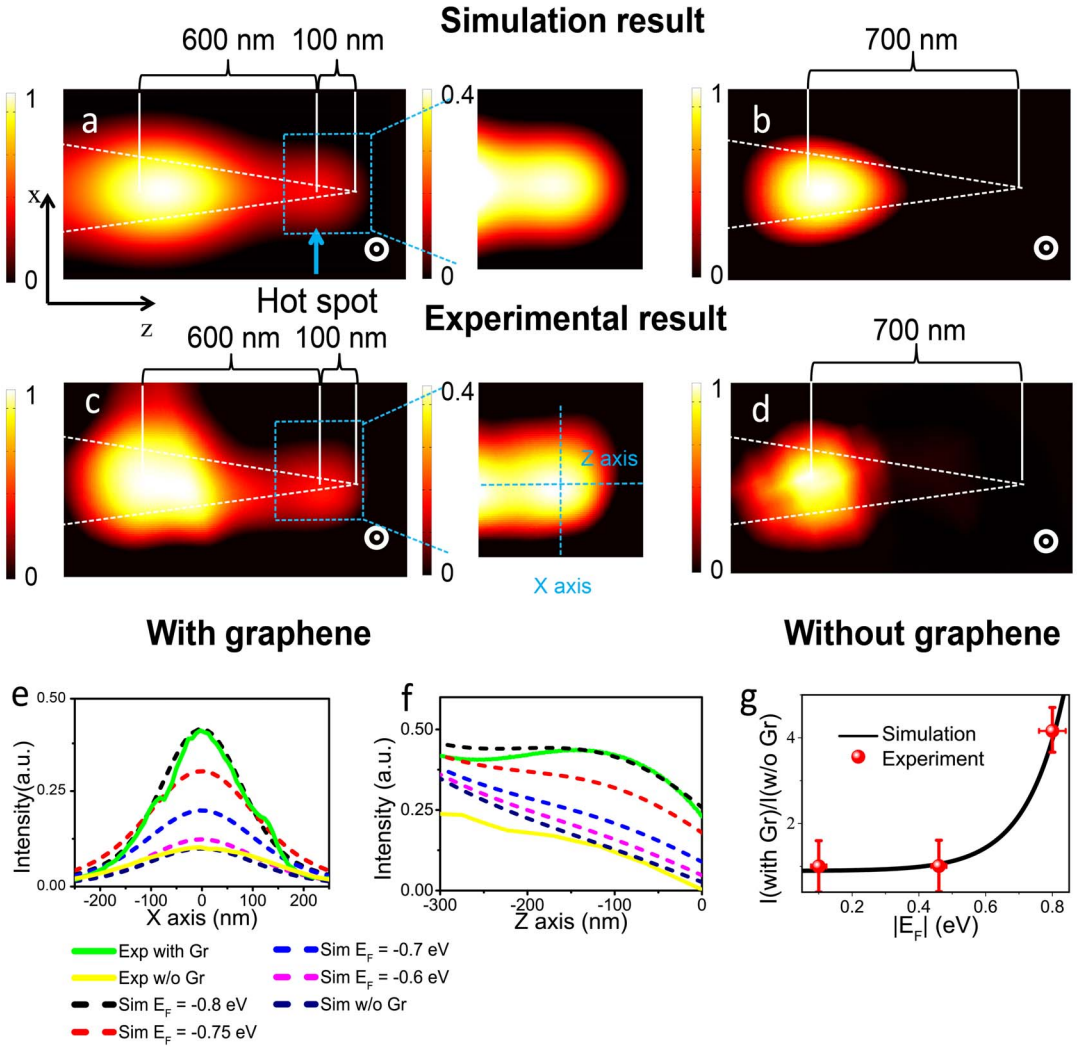

Figure 4 | Near-field images of the tapered graphene-silicon waveguide tip. Simulation (a, b) with the convolution of the point-spread function of NSOM probes and experimental results (c, d) of the tapered graphene-silicon waveguide tips with (a, c) and without (b, d) the doped graphene layer under TM polarization illumination, respectively. The input polarization direction is indicated on the bottom right corner. Cross section of the hot spot along x (e) and z (f) axis near the end of the tip in the experimental result and simulation result of the tapered graphene-silicon waveguide tips. (g). Simulation and experimental result of the intensity ratio of the hot spot compared with the sample without graphene (I(with Gr)/I(w/o Gr)).

1. Castro Neto, A. H., Guinea, F., Peres, N. M. R., Novoselov, K. S. & Geim, A. K. The electronic properties of graphene. *Rev Mod Phys* **81**, 109–162 (2009).
2. Jablan, M., Buljan, H. & Soljacic, M. Plasmonics in graphene at infrared frequencies. *Phys Rev B* **80**, 245435 (2009).
3. Mikhailov, S. A. & Ziegler, K. New electromagnetic mode in graphene. *Phys Rev Lett* **99**, 016803 (2007).
4. Grigorenko, A. N., Polini, M. & Novoselov, K. S. Graphene plasmonics. *Nat Photonics* **6**, 749–758 (2012).
5. Low, T. & Avouris, P. Graphene Plasmonics for Terahertz to Mid-Infrared Applications. *Acs Nano* **8**, 1086–1101 (2014).
6. Koppens, F. H. L., Chang, D. E. & de Abajo, F. J. G. Graphene plasmonics: a Platform for strong light-matter interactions. *Nano Lett* **11**, 3370–3377 (2011).
7. García de Abajo, F. J. Graphene plasmonics: challenges and opportunities. *ACS Photonics* **1**, 135–152 (2014).
8. Bao, Q. L. & Loh, K. P. Graphene photonics, plasmonics, and broadband optoelectronic devices. *Acs Nano* **6**, 3677–3694 (2012).
9. Vakil, A. & Engheta, N. Transformation optics using graphene. *Science* **332**, 1291–1294 (2011).
10. Kim, J. T. & Choi, S. Y. Graphene-based plasmonic waveguides for photonic integrated circuits. *Opt Express* **19**, 24557–24562 (2011).
11. Ju, L. *et al.* Graphene plasmonics for tunable terahertz metamaterials. *Nat Nanotechnol* **6**, 630–634 (2011).
12. Chen, J. N. *et al.* Optical nano-imaging of gate-tunable graphene plasmons. *Nature* **487**, 77–81 (2012).
13. Fei, Z. *et al.* Gate-tuning of graphene plasmons revealed by infrared nano-imaging. *Nature* **487**, 82–85 (2012).
14. Yan, H. G. *et al.* Damping pathways of mid-infrared plasmons in graphene nanostructures. *Nat Photonics* **7**, 394–399 (2013).
15. Brar, V. W. *et al.* Hybrid surface-phonon-plasmon polariton modes in graphene/monolayer h-BN heterostructures. *Nano Lett* **14**, 3876–3880 (2014).
16. Li, Y. L. *et al.* Graphene plasmon enhanced vibrational sensing of surface-adsorbed layers. *Nano Lett* **14**, 1573–1577 (2014).
17. Liu, F. & Cubukcu, E. Tunable omnidirectional strong light-matter interactions mediated by graphene surface plasmons. *Phys Rev B* **88**, 115439 (2013).
18. Geim, A. K. & Novoselov, K. S. The rise of graphene. *Nat Mater* **6**, 183–191 (2007).
19. Chen, C. F. *et al.* Controlling inelastic light scattering quantum pathways in graphene. *Nature* **471**, 617–620 (2011).
20. Liu, H., Liu, Y. & Zhu, D. Chemical doping of graphene. *J Mater Chem* **21**, 3335–3345 (2011).
21. Shao, Y. Y. *et al.* Nitrogen-doped graphene and its electrochemical applications. *J Mater Chem* **20**, 7491–7496 (2010).
22. Khrapach, I. *et al.* Novel highly conductive and transparent graphene-based conductors. *Adv Mater* **24**, 2844–2849 (2012).
23. Chen, Z. Y. *et al.* Surface transfer hole doping of epitaxial graphene using MoO3 thin film. *Appl Phys Lett* **96**, 213104 (2010).
24. Xie, L. F. *et al.* Electrical measurement of non-destructively p-type doped graphene using molybdenum trioxide. *Appl Phys Lett* **99**, 012112 (2011).
25. Pisana, S. *et al.* Breakdown of the adiabatic Born-Oppenheimer approximation in graphene. *Nat Mater* **6**, 198–201 (2007).
26. Lazzeri, M. & Mauri, F. Nonadiabatic Kohn anomaly in a doped graphene monolayer. *Phys Rev Lett* **97**, 266407 (2006).

27. Ferrari, A. C. *et al.* Raman spectrum of graphene and graphene layers. *Phys Rev Lett* **97**, 187401 (2006).
28. Oulton, R. F., Sorger, V. J., Genov, D. A., Pile, D. F. P. & Zhang, X. A hybrid plasmonic waveguide for subwavelength confinement and long-range propagation. *Nat Photonics* **2**, 496–500 (2008).
29. Dai, D. X. & He, S. L. A silicon-based hybrid plasmonic waveguide with a metal cap for a nano-scale light confinement. *Opt Express* **17**, 16646–16653 (2009).
30. He, X. L., Yang, L. & Yang, T. Optical nanofocusing by tapering coupled photonic-plasmonic waveguides. *Opt Express* **19**, 12865–12872 (2011).
31. Thongrattanasiri, S., Manjavacas, A. & de Abajo, F. J. G. Quantum finite-size effects in graphene plasmons. *Acs Nano* **6**, 1766–1775 (2012).
32. Das, A. *et al.* Monitoring dopants by Raman scattering in an electrochemically top-gated graphene transistor. *Nat Nanotechnol* **3**, 210–215 (2008).
33. Lazzeri, M. & Mauri, F. Nonadiabatic Kohn anomaly in a doped graphene monolayer. *Phys Rev Lett* **97**, 266407 (2006).
34. Zolyomi, V., Koltai, J. & Kurti, J. Resonance Raman spectroscopy of graphite and graphene. *Phys Status Solidi B* **248**, 2435–2444 (2011).
35. Ozbay, E. Plasmonics: Merging photonics and electronics at nanoscale dimensions. *Science* **311**, 189–193 (2006).
36. Agrawal, G. P. *Fiber-Optic Communication Systems.* (Wiley, 2012).
37. Kawata, S., Inouye, Y. & Verma, P. Plasmonics for near-field nano-imaging and superlensing. *Nat Photon* **3**, 388–394 (2009).
38. Jain, P. K., Huang, X. H., El-Sayed, I. H. & El-Sayed, M. A. Noble metals on the nanoscale: optical and photothermal properties and some applications in imaging, sensing, biology, and medicine. *Accounts Chem Res* **41**, 1578–1586 (2008).
39. Zijlstra, P., Chon, J. W. M. & Gu, M. Five-dimensional optical recording mediated by surface plasmons in gold nanorods. *Nature* **459**, 410–413 (2009).
40. Li, X., Zhang, Q., Chen, X. & Gu, M. Giant refractive-index modulation by two-photon reduction of fluorescent graphene oxides for multimode optical recording. *Sci Rep* **3**, 2819 (2013).
41. Gorbach, A. V. Nonlinear graphene plasmonics: amplitude equation for surface plasmons. *Phys Rev A* **87**, 013830 (2013).
42. Hendry, E., Hale, P. J., Moger, J., Savchenko, A. K. & Mikhailov, S. A. Coherent nonlinear optical response of graphene. *Phys Rev Lett* **105**, 097401 (2010).
43. Gusynin, V. P., Sharapov, S. G. & Carbotte, J. P. Unusual microwave response of Dirac quasiparticles in graphene. *Phys Rev Lett* **96**, 256802 (2006).
44. Peres, N. M. R., Guinea, F. & Neto, A. H. C. Electronic properties of disordered two-dimensional carbon. *Phys Rev B* **73**, 125411 (2006).

Acknowledgments

M.G. acknowledges the support from the Australian Research Council (ARC) Laureate Fellowship program (FL100100099). This work was supported in part by the ARC Centre for Ultrahigh-bandwidth Devices for Optical Systems (CUDOS) (project number CE110001018). Q.B. acknowledges the support from 863 Program (2013AA031903), the NSFC Grants (51222208, 51290273), ARC DECRA (DE120101569), DP (DP140101501). This work was performed in part at the Melbourne Centre for Nanofabrication (MCN) in the Victorian Node of the Australian National Fabrication Facility (ANFF). S.F. acknowledges the support of an AFOSR-MURI program on Integrated Hybrid Nanophotonic Circuits (Grant No. FA9550-12-1-0024).

Author contributions

Q.Z., X.L., Q.B. and M.G. proposed the idea and the strategy for experimental design, analysed the data and completed the writing of the paper. Q.Z. performed fabrication, numerical simulation and near-field characterization. M.M.H. performed numerical simulation and contributed to writing the manuscript. Y.X. and J.Z. contribute to deposition of MoO_3 thin film and UPS/AFM characterizations, J.S. and J.L. contribute to graphene growth, transfer and Raman characterizations. M.D.T. and S.F. contributed to analyse the data.

Additional information

Supplementary information accompanies this paper at http://www.nature.com/scientificreports

Competing financial interests: The authors declare no competing financial interests.

How to cite this article: Zhang, Q. *et al.* Graphene surface plasmons at the near-infrared optical regime. *Sci. Rep.* **4**, 6559; DOI:10.1038/srep06559 (2014).